UCRL-ID-138913

Transmutation of Radioactive Nuclear Waste

A. Toor, R. Buck

March 15, 2000

U.S. Department of Energy

Lawrence
Livermore
National
Laboratory

DISCLAIMER

This work was performed under the auspices of the U. S. Department of Energy by the University of California, Lawrence Livermore National Laboratory under Contract No. W-7405-Eng-48.

Transmutation of Radioactive Nuclear Waste

99-FS-008
A. Toor, R. Buck
March 15, 2000

Introduction

Lack of a safe disposal method for radioactive nuclear waste (RNW) is a problem of staggering proportion and impact. A typical LWR fission reactor will produce the following RNW in one year: minor actinides (i.e. ^{237}Np, $^{242\text{-}243}$Am, $^{243\text{-}245}$Cm) ~40 kg, long-lived fission products (i.e, ^{99}Tc, ^{93}Zr, ^{129}I, ^{135}Cs) ~80 kg, short lived fission products (e.g. ^{137}Cs, ^{90}Sr) ~50kg and plutonium ~ 280 kg. The total RNW produced by France and Canada amounts to hundreds of metric tonnes per year [1]. Obtaining a uniform policy dealing with RNW has been blocked by the desire on one hand to harvest the energy stored in plutonium to benefit society and on the other hand the need to assure that the stockpile of plutonium will not be channeled into future nuclear weapons [2, 3].

In the meantime, the quantity and handling of these materials represents a potential health hazard to the world's population and particularly to people in the vicinity of temporary storage facilities. In the U.S., societal awareness of the hazards associated with RNW has effectively delayed development of U.S. nuclear fission reactors during the past decade. As a result the U.S. does not benefit from the large investment of resources in this industry. Reluctance to employ nuclear energy has compelled our society to rely increasingly on non-reusable alternative energy sources; coal, oil, and natural gas. That decision has compounded other unresolved global problems such as air pollution, acid rain, and global warming. Relying on these energy sources to meet our increasing energy demands has led the U.S. to increase its reliance on foreign oil; a policy that is disadvantageous to our economy and our national security.

RNW can be simplistically thought of as being composed of two principal components: 1) actinides with half lives up to 10^6 years and 2) the broad class of fission fragments with typical half lives of a few hundred years. One approach to the RNW storage problem has been to transmute the radioactive elements into other radioactive isotopes with much shorter half-lives. Transmutation of both RNW components using neutrons has been discussed and studied over the past four decades. Most transmutation studies have examined the feasibility of using neutron-induced reactions where the neutrons would be provided by accelerator-based spallation neutron sources, tokamak fusion reactors, sub-critical fission reactors and other novel concepts [4, 5, 6]. Studies have shown that all proposed transmutation processes to treat RNW using neutron reactions are deficient or marginal at best from the point of view of energy consumption and/or cost. We suggest an alternative approach that has not been considered to date: the transmutation of RNW elements using high-energy photons or gamma rays.

The photo-disintegration of RNW may provide an effective way to treat reprocessed waste; waste that has been chemically separated or the residual waste left over after neutron processing. Photo-disintegration is attractive in that any isotope can be transmuted. This approach is now potentially practical because of the development of micropole undulators (MPUs) [7] that allow us to use small storage rings to economically generate photons with gamma-ray energies and to tune these "gamma rays" to the peak of the cross-section resonance for various RNW elements. Because the cross sections for all RNW nuclei have a broad peak with the maximum in the 12-18 MeV range, a single MPU could be used to treat both actinide and fission fragment components of RNW.

The goal of this study is to make estimates of the reaction rates and energy efficiency of the transmutation of typical RNW elements using gamma rays to establish whether or not gamma-ray transmutation should be examined as a viable alternative solution to RNW warranting further study.

Procedure

In this study we examined the photon-mediated transmutation of ^{137}Cs and ^{90}Sr, two major components of RNW with half-lives of about 30 years. At 14 MeV, both species undergo (gamma,n) reactions, producing daughter isotopes with half-lives of 13 and 50 days, respectively. At higher photon energies, photo-fission in addition to the (gamma,n) reactions takes place. The fission products (fission fragments and secondary neutrons) cause further transmutation of the RNW.

We used the LLNL 3-D Monte Carlo code COG [8] to simulate the transmutation process. COG solves the Boltzmann equation for the transport of neutrons and photons, and links to the EGS [9] electron transport code kernel for the transport of electrons. In addition, COG has many variance reduction techniques that enable it to solve difficult deep-penetration shielding and transport problems. It does not, however, have the capability at present to create and track the fission products and account for their subsequent interactions. We therefore limited the scope of this study to simulate only the (gamma,n) reactions due to a 14-MeV photon beam interacting in a target which was either pure ^{137}Cs or ^{90}Sr. An example of a COG input deck is given in Appendix A.

We used the giant dipole cross section ,

$$\sigma = \frac{40E_\gamma^2\pi(A-Z)Z\alpha\Gamma\frac{h}{2\pi}c^2}{AM\left[E_\gamma^4 + E_r^4 + E_\gamma^2\left(\Gamma^2 - 2E_r^2\right)\right]}$$

where E_r is the resonance energy, Γ is the resonance width, E_γ is the photon energy, M is 938.27 MeV, $(h/2\pi)c^2$ is 197.329 and α is 1/137.036. For the cases we studied the resonance energy and width can be approximated by: $E_r = \frac{80}{\sqrt[3]{A}} MeV$, and Γ = 5 MeV.

The resonance energies for ^{90}Sr and ^{137}Cs are 17.8 MeV and 15.5 MeV respectively. The (gamma,n) branch dominates the total cross section (>90%). The giant dipole resonance cross sections for ^{90}Sr and ^{137}Cs are given in Fig. 1.

The geometry used in our simulations was a pencil beam of 14-MeV photons directed along the axis to one end of a large right cylinder of ^{90}Sr or ^{137}Cs. The radius and length of the cylinder were 20 cm and 100 cm respectively. These dimensions were large enough to stop the entire photon beam. The photon flux and reaction rates were calculated using two types of detectors to tabulate the results; surface, or boundary crossing (BC) detectors and volume, or reaction detectors. Each photon crossing a BC detector boundary contributed to the flux recorded for the detector in units of photons/cm^2. For a reaction detector, the collision density of photons traversing the detector volume was used to compute an average flux over the entire detector volume. We calculated the flux, $\Phi(E)$, using both BC and reaction detectors. The specific (gamma,n) reaction rate is given by:

$$\frac{dN}{dT} = S \cdot \sum_j \left[\Phi_{E_j} \rho \sigma_{E_j} \frac{N_0}{A} \right]$$

where the units are reactions/(cm^3-s). Here S is the source strength (photons/s), ρ is the material density (g/cm^3), σ_{Ej} is the (gamma,n) atomic cross section (cm^2) at energy E_j, N_o is Avogadro's number and A is the atomic weight (g/mole) and the sum is taken over all scoring particles. If Φ is tallied using a reaction detector, multiplying the reaction rate as defined above by the detector volume gives the total number of (gamma,n) reactions in the volume per source particle (src). It is convenient to define the normalized reaction rate R as

$$R = \frac{1}{S} \cdot \frac{dN}{dT}$$

with units (reactions/cm^3-src) so the results can be readily scaled for any specified source. This is the quantity we computed in our studies.

^{137}Cs Results

The reaction rate vs. depth in ^{137}Cs for a 100,000-particle run is shown in Table 1. For all Cs runs, we used the normal metalic density (1.88 g/cm^3).

Table 1.
^{137}Cs (gamma,n) reaction rate vs. depth. 100,000 histories

Depth (cm)	Reactions /(cm^3-src)	Fractional Standard Deviation
0	1.21E-06	8.25E-09
5	8.01E-07	2.26E-03
10	5.31E-07	3.56E-03

20	2.34E-07	6.41E-03
30	1.04E-07	1.02E-02
40	4.58E-08	1.57E-02
60	9.15E-09	3.55E-02
80	1.71E-09	8.20E-02
100	3.36E-10	1.84E-01

The integral of the specific reaction rate over the distance into the target gives 1.53×10^{-5} reactions/(cm^2-src). This implies a mean reaction rate of 1.53×10^{-5} reactions/(cm^3-src). The net reaction rate is 1.53×10^{-5} times the target cross section (1.26×10^3 cm^2) which gives 0.0192 reactions/(src) or about 2% of the incident beam. A similar net reaction rate is obtained from the volume reaction detector (0.0185). Therefore, integrating over the entire volume gives 1.9×10^{-2} (gamma, n) reactions per source particle whereas it is seen from Table 1 that the reaction rate for the first few centimeters is a factor of ~4 higher.

^{90}Sr Results

We used same cylindrical geometry with a pencil beam of 14-MeV gamma rays to simulate the transmutation of ^{90}Sr. The normal metalic density for Sr (2.54 g/cm^3) was used. One hundred thousand gamma-ray histories were tabulated to obtain the average reaction rate from both volume and surface crossing detectors in the same manor that was used for the ^{137}Cs simulation. Results from this simulation are shown in Table 2.

Table 2.
^{90}Sr (gamma,n) reaction rate vs. depth. 100,000 histories

Depth (cm)	Reactions /(cm^3-src)	Fractional Standard Deviation
0	7.17×10^{-8}	7.38×10^{-9}
5	4.58×10^{-8}	2.36×10^{-3}
10	2.92×10^{-8}	3.78×10^{-3}
20	1.19×10^{-8}	7.00×10^{-3}
30	4.83×10^{-9}	1.16×10^{-2}
40	1.92×10^{-9}	1.86×10^{-2}
60	3.16×10^{-10}	4.56×10^{-2}
80	4.57×10^{-11}	1.19×10^{-1}
100	8.53×10^{-12}	2.74×10^{-1}

The reaction rate as determined by the volume detector was 2.45×10^{-4} particles/(cm^2-src). When summed over thickness the specific reaction rate obtained was 8.00×10^{-9} reactions/(cm^3–src). The average reaction rate obtained by integrating the specific reaction rate over the volume (1.26×10^5 cm^3) was 1.01×10^{-3} reactions per source particle. Using the data in Table 2 one obtains the integral of the specific reaction rate over the depth of the target to be 8.31×10^{-7} reactions/(cm^2-src). This implies a mean reaction rate of 8.31×10^{-9} reactions/(cm^3-src) which is not significantly different from that obtained above from the volume detector. Multiplying the mean reaction rate by the target cross section area (1.26×10^3 cm^2) one obtains the net reaction rate for 14 MeV gamma rays in ^{90}Sr of 0.0010 reactions per source particle.

For both ^{137}CS and ^{90}Sr we find that >97% of gamma-ray interactions are atomic reactions, namely Compton scattering and pair-production and only a few percent are nuclear reactions. The electrons and positrons resulting from the atomic reactions are the major source of energy loss limiting the gamma ray induced transmutation efficiency. It is clear that even if more detailed simulations that include photo-fission processes and that track the subsequent transmutations due to fission fragments and secondary neutrons show factors of 4-5 improvement in the transmutation rates, hope for this technological solution to RNW will require the development of a capability to recover a significant fraction (~30%) of the energy carried by the Compton electrons.

Certain applications have used inverse Klystrons that convert >60% of the energy carried by the electrons to electricity. Capture and reuse of this energy in a transmutation plant could make the difference between the concept being economically feasible or infeasible. One possible geometry to treat RNW would be a stack of thin (~ cm) disks of RNW separated by gaps containing inverse Klystrons or similar devices.

Stacks of ^{137}Cs disks

To examine the possibility of extracting energy from the electrons and positrons, several COG simulations were run with stacks of ^{137}Cs in the form of thin disks separated from each other by a vacuum gap. The thickness of the ^{137}Cs disks in these simulations ranged from 2 cm down to 0.1 cm. The systematics of the 1-cm and 2-cm thick disk runs are summarized in Tables 3 and 4. The geometry for these runs was a stack of five disks separated by 5-cm vacuum gaps. The surface crossing detectors were angle masked to score only forward-directed particles. Table 3 lists the forward directed particles emitted from the back surface of each disk for 1-cm thick disk. The numbers listed refer to particles, not flux, i.e. the data have not been divided by the normal area. The data have, however, been normalized per source particle (src).

Table 3.
A Stack of 1-cm Thick Disks of Cs137 separated by 5-cm Vacuum

Disk Number	e+, e- Energy Out of Back Surface (MeV/(src)	Photon Energy Out of Back Surface (Mev/src)	Unscattered 14-Mev Photon Fraction	Number of Conversion Reactions/src
1	0.61	13.03	0.92	1.40×10^{-3}
2	0.68	12.21	0.85	1.30×10^{-3}
3	0.64	11.43	0.78	1.18×10^{-3}
4	0.59	10.68	0.72	1.10×10^{-3}
5	0.54	9.97	0.66	1.01×10^{-3}

The data in Table 3 show the unscattered fraction of gamma rays that left the back surface of the first 1-cm thick disk was 92%. Eight percent of the gamma rays interacted in the disk of which ~ 0.14% resulted in (gamma,n) nuclear conversions with the balance of interactions being atomic; Compton scattering and pair production. The energy carried by electrons and positrons out of the back surface corresponds to 0.61 MeV per source particle; a value that corresponds to over one half of the total energy of the interacting photons.

It is interesting to note (see Table 3) that after the gamma-ray beam has passed through 5 cm of material, the energy carried by photons out of the back surface is ~ 10 MeV per incident photon and the energy carried by the electrons into the vacuum behind each disk is 3 MeV per incident photon. Together this accounts for 93% of the total energy. The remaining 7% of the energy is shared between the kinetic energy of electrons and positrons escaping from the front surfaces of the disk and that which has gone into material temperature.

Table 4 summarizes the information from a similar 100,000 particle (14-MeV photon) run with the five, 2-cm thick ^{137}Cs disks. Again, a 5-cm vacuum gap separated each disk from its neighbors. The data in Table 4 exhibits the same trend that was seen in Table 3 but the energy carried by the electrons and positrons into the vacuum gaps behind each of the 5 disks decreased from one-half to one-third of the total energy of the interacting photons.

Table 4
A Stack of 2-cm Thick Disks of ^{137}Cs separated by 5-cm Vacuum

Disk Number	e+, e- Energy Out of Back Surface (MeV/(src)	Photon Energy Out of Back Surface (Mev/src)	Unscattered 14-Mev Photon Fraction	Conversion Reactions/src
1	0.69	12.22	0.85	2.59×10^{-3}
2	0.59	10.72	0.72	2.19×10^{-3}
3	0.51	9.37	0.61	1.86×10^{-3}
4	0.44	8.16	0.51	1.58×10^{-3}
5	0.37	7.08	0.43	1.34×10^{-3}

Stack of 50 ^{137}Cs 0.5 cm thick disks

To estimate the total energy transported into the vacuum gaps by electrons and positrons, we ran a COG simulation with 100,000 photons for a stack of fifty 0.5 cm thick disks; each separated by a 5-cm vacuum gap. The disk radii were 20 cm. The data from this run is summarized in Fig. 2 and Fig. 3 and is presented in tabular form in Appendix B. That there is more net energy in the outgoing electrons and positrons than in the source indicates we double counted some of the particles in this simulation. Because of the thin (0.5 cm) disks, a fraction of the positrons that emerged from any disk could create photon-electron cascades in the subsequent disk and some products of these cascades emerged and were counted in the next gap. The magnitude of the effect is seen to be small and such double counting does not alter the conclusions drawn from our simulations.

The energy per source particle associated with photons emerging into the vacuum gaps is shown in Fig. 2. The total energy per source particle due to both scattered and unscattered photons is compared with the energy associated with the unscattered photons only. These data show that the ratio of the total energy associated with photons to the

unscattered photon energy monotonically increases from 1.00 in the first vacuum gap to 1.13 in the last. Figure 2 also gives the energy per source particle of the electrons and positrons leaving the back surfaces of the disks. Throughout the stack, the photons emerging into any vacuum gap are seen to account for 18-20 times more energy than that associated with the Compton electrons and electrons and positrons resulting from pair production that emerge into the gap.

The number of nuclear transmutations per atomic reaction in ^{137}Cs is shown in Fig 3. These data show the same trends and features that are seen in Tables 1 and 2. It is seen from these data and the data in Appendix A that the number of unscattered photons per source particle is ~ 10^3 times higher than the number of nuclear transmutations per source particle.

Electron Spectrum and Angular Distribution

Whether or not this overall transmutation efficiency is high enough to make treatment of RNW with gamma rays competitive with neutron transmutation will depend to a large degree on the ability to re-convert to electrical energy the energy carried by the electrons and positrons created in the RNW. The conversion efficiency of electron kinetic energy to current in turn depends on the angular distributions and energy distributions of the electrons and positrons. Figures 4 and 5 show the results of a $3x10^6$ history simulation of a 1-mm thick ^{137}Cs disk that was illuminated with a 14 MeV beam of photons. The properties of the electrons and positrons were tallied in a BC detector located at the rear vacuum interface of the disk. The electron and positron energy spectra are compared in Fig. 5. The ordinate units are particles/(cm^2 • src). Approximately 0.1% of the source photons interact in the 1-mm disk therefore, the flux of electrons and positrons emitted from the backside of the disk corresponds to 100 particles per cm^2 for every transmutation. The emerging positrons and electrons are seen to be contained in a 20-degree FWHM cone and have a mean energy of ~ 3.5 MeV.

Conclusions

We are not aware of any technologies that can extract a significant fraction of the energy of the electrons as described above. We conclude that although the physics associated with the proposed gamma-ray transmutation scheme is sound, there remain major obstacles that need to be overcome if one is to treat large volumes of RNW economically. Development of an inverse Klystron or similar device to capture a significant fraction (~30%) of the energy carried by the Compton electrons will be required to make the scheme energetically feasible. Without a RF field, the positrons coming off the back surfaces of the disks become problematic for schemes that would extract the DC energy from the electrons. Even if an efficient energy extraction system could be realized, our calculations show it will be necessary to have sub-cm thick disks to transport a significant fraction of the electrons out of the RNW. It appears to us that this requirement will make the costs associated with processing and handling the RNW wasteform too high to become a realized practical solution for the treatment of RNW.

Nonetheless, there may still be an important role for photon-mediated transmutation of specific isotopes that are especially refractory in the neutron transmutation processes. Unlike neutron transmutation schemes, all RNW isotopes can be transmuted into isotopes with shorter half-lives through the (gamma,n) process. Therefore the benefit of being able to transmute specific troublesome isotopes may outweigh the costs associated with their reprocessing and handling. For such cases, optimization of the RNW geometry to provide the highest overall transmutation efficiency could be readily calculated.

Figure 1. The Giant Dipole Resonance cross section for ^{137}Cs (a) and ^{90}Sr (b).

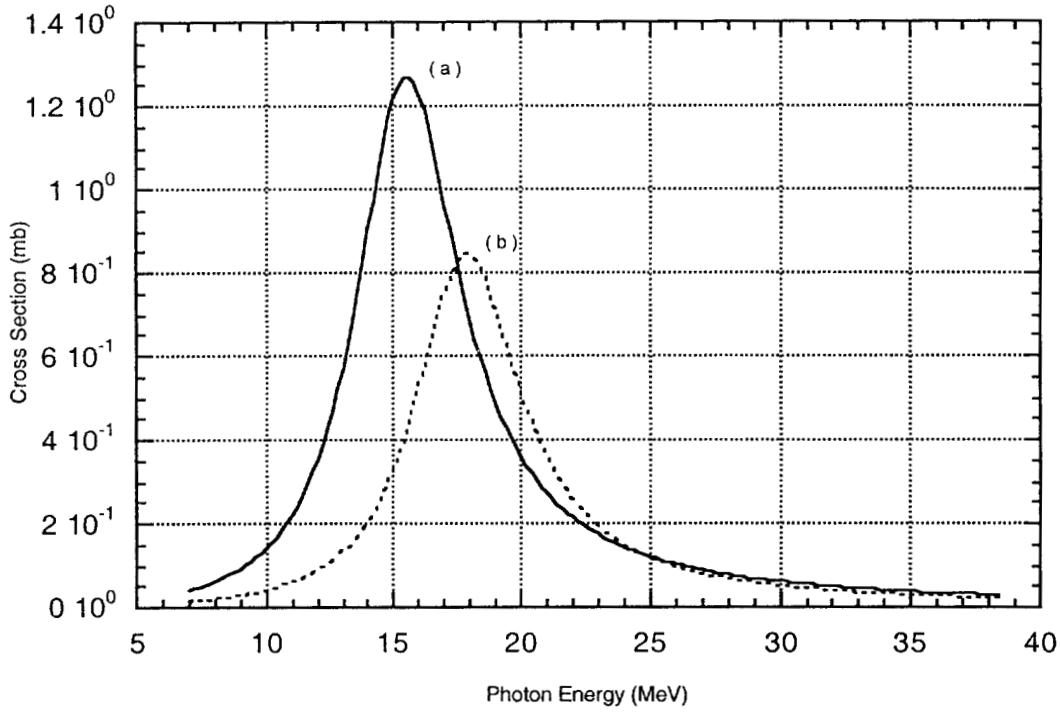

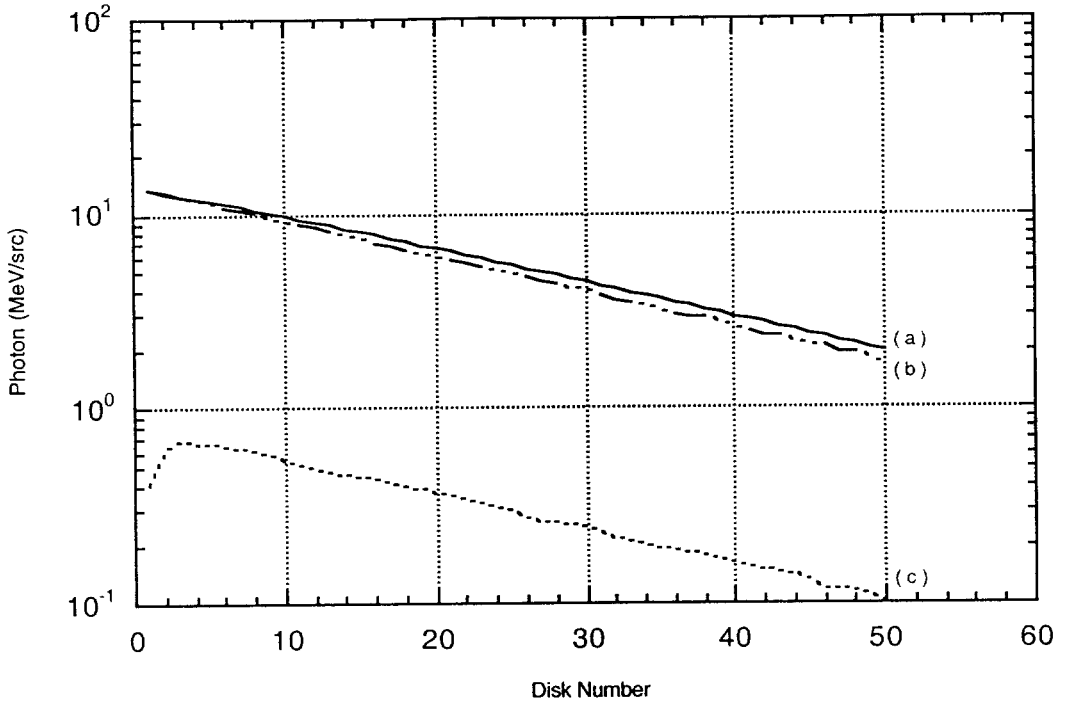

Figure 2. The energy associated with the photons and electrons emerging into vacuum gaps separating a stack of fifty ^{137}Cs disks. The energy of the scattered plus uncattered photons (a) is compared with the unscattered photons only (b). The values for electrons (c) include the contribution from both electrons and positrons. Five-centimeter vacuum gaps separated the 20-cm radius, 0.1 cm thick disks.

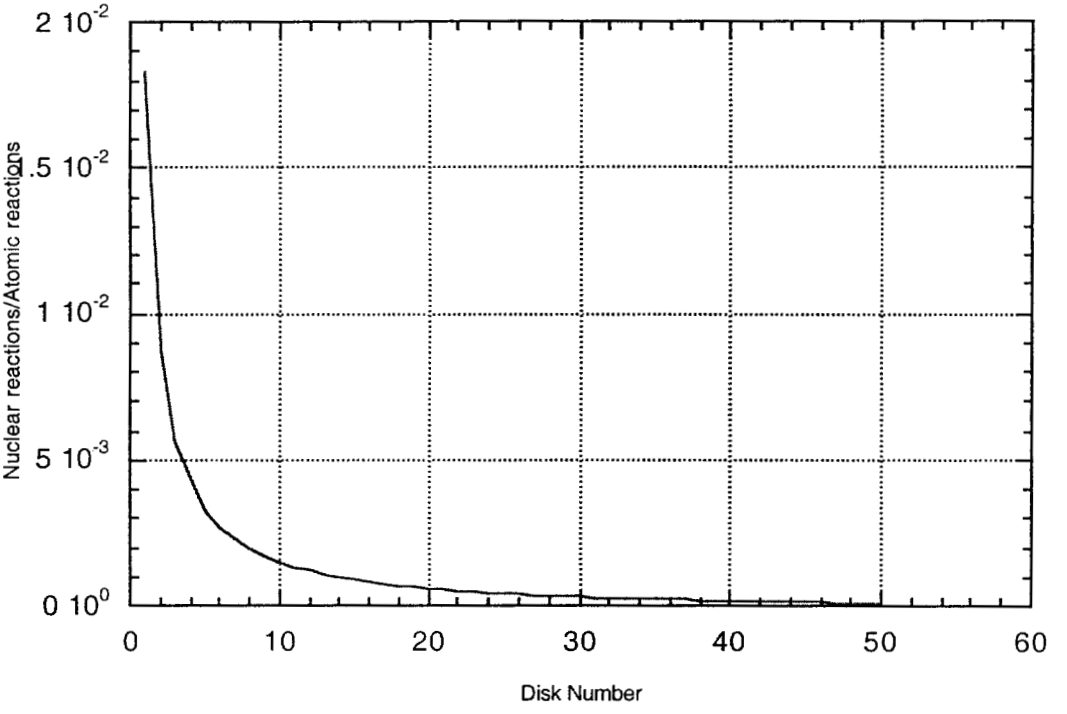

Figure 3 The number of nuclear transmutations per atomic reaction (pair production and Compton Scattering) for 14-MeV photons interacting in ^{137}Cs. The thickness for each disk was 0.1 cm and a 5-cm vacuum gap was behind each disk.

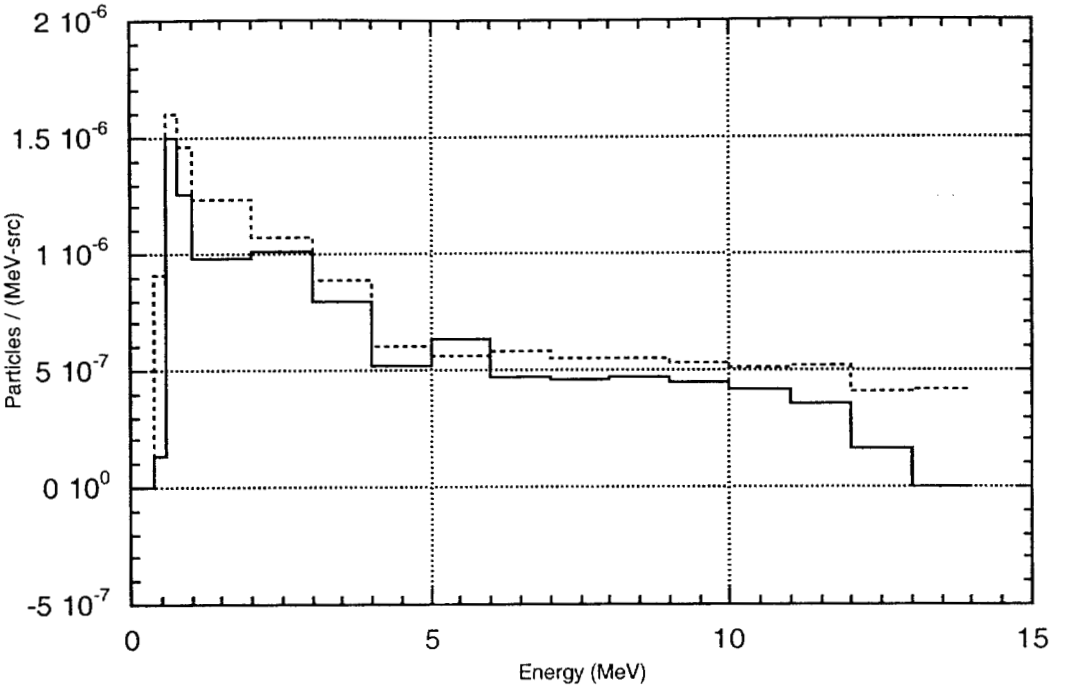

Figure 4. The energy spectra for positrons (solid curve) and electrons (dashed curve) emerging from the back side of a 1 mm thick ^{137}Cs plate. The simulation tallied three million 14-Mev photon histories.

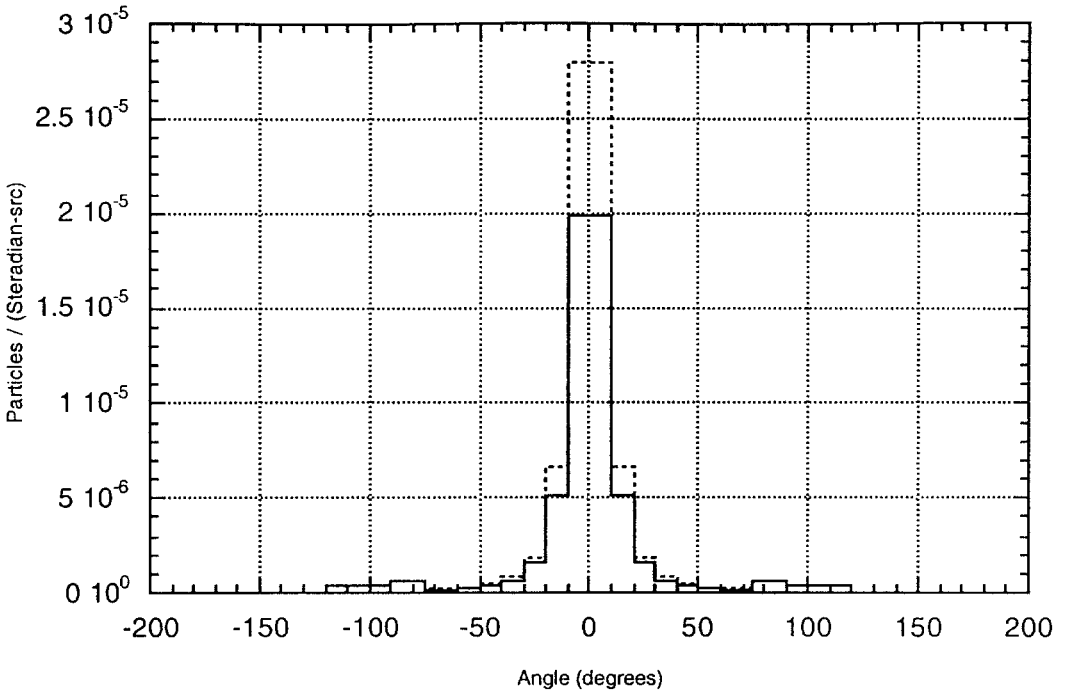

Figure 5. Angular distribution of electrons (dashed) and positrons (solid) emitted from the back surface of a 1-mm thick ^{137}Cs plate. The source was a pencil beam of 14 MeV photons.

References

1. R. B. Stout, H. R. Leider, "Waste Form Characteristics Report - Revision 1", LLNL report UCRL-ID-108314 Version 1.2, (1997).

2. F. Von Hipple, "Eliminating Nuclear Warheads", *Scientific American*, (August 1993)

3. J. P. Holdren (Ed), "Management and Disposition of Excess Weapons Plutonium", National Academy of Sciences (National Academy Press, Washington, DC, 1994)

4. L. C. Hebel et al., *Rev. Mod. Phys.* 50, 1 (1978)

5. C. D. Bowman et al., *Nucl. Instr. Meth. In Phys. Research*, A320,336 (1992)

6. F. Venneri et al., *Physics World*, No. 8, 40 (August 1993).

7. R.Tatchyn, A. Toor, J. Hunter, R. Hornady, D. Whelan, G. Westenskow, P. Csonka, T. Cremer, and E. Kallne, *X-ray Science and Technology*, 1, (1),79, (1989).

8. T. P. Wilcox, Jr., and E. M. Lent, "COG - A Particle Transport Code Designed to Solve the Boltzmann Equation for Deep-Penetration (Shielding) Problems. Vol. 1: User Manual", LLNL Rept. M-221-1 (1989).

9. W.R. Nelson, H. Hirayama, and D.W.O. Rogers, "The EGS4 Code System", SLAC-Report-265, December 1985.

Appendix A

An example of a COG input deck used in these simulations.

```
csst5.2: Cesium 137 (gamma,n) Transmutation problem 2/11/00
$ Stack of 5 2-cm Cs plates, followed by a 5 cm vacuum gap.
$ Apply angle mask to score only forward-directed flux.

$ SOURCE: 14 MeV photons
$ photon MFP at 14 MeV: 12 cm
$ Fraction emerging unscattered afer 1 cm: 0.92
$ Fraction emerging unscattered afer 5 cm: 0.66
$  Electron Range
$  E (MeV)  R(cm)
$   10.   3.2
$    5.   1.9
$    1.   0.4
$    0.5  0.2
$ Using revised Cs137 (g,n) detector response function from K Sale.
$ 9/22/99

$ We use a detector DRF-E of [rho0*sigma*Na/A] (inverse cm)
$  to convert detector flux to (gamma,n) reaction rate:
$ RR = f* phi * [rho0*sigma*Na/A]  in units of # of reactions/(cm^3-sec).
$ where:
$  phi = flux (particles/cm^2-sec);
$  f   = density multiplier;
$  rho0 = nominal density (1.88 gm/cm^3);
$  sigma = (gamma,n) cross section (cm^2/atom)
$  Na    = Avogadro's #;
$  A     = atomic weight (gm)


BASIC
  photon electron
  RN 11 4
  NOFINALRESTART

MIX
    mat 1 cs 1.88

SURFACES
    200 cyl 20. -2. 150.
   1000 plane x  0.  $ Begin CS 1
```

```
 1 plane x  2.  $ Begin gap
11 plane x  7.  $ Begin CS 2
12 plane x  9.  $ Begin gap
13 plane x 14.  $ Begin CS 3
14 plane x 16.  $ Begin gap
15 plane x 21.  $ Begin CS 4
16 plane x 23.  $ Begin gap
17 plane x 28.  $ Begin CS 5
18 plane x 30.  $ Begin gap
19 plane x 35.  $ Endgap

999 cyl 25. -10. 200.


GEOMETRY
 sector 10 src     -200 -1000
 sector 11 cs1     -200 +1000  -1
 sector 12 gap1    -200 +1  -11
 sector 13 cs2     -200 +11 -12
 sector 14 gap2    -200 +12 -13
 sector 15 cs3     -200 +13 -14
 sector 16 gap3    -200 +14 -15
 sector 17 cs4     -200 +15 -16
 sector 18 gap4    -200 +16 -17
 sector 19 cs5     -200 +17 -18
 sector 20 gap5    -200 +18 -19

 sector 40 ext     +200 -999
 boundary vacuum +999

ASSIGN-ML
 1 11 13 15 17 19  /
 0 10 12 14 16 18 20 40

 SOURCE
  NPART 100000
  DEFINE P=1
  POINT -1. 0. 0.
  DEFINE E=1
  PHOTON LINE 14. 1.
  DEFINE A=1
  1. 0. 0. FIXED

 INCREMENT 1.0 P=1 E=1 A=1
```

```
EGS
 PEGSLIB =  Cs.dat
 ESECTORS = 10 11 12 13 14 15 16 17 18 19 20


DETECTOR
 NUMBER = BC_ET1
 boundary COUNTS 11 12 1256.64
 MASK-E photon 0. 0.
 MASK-A 1. 0. 0.  0. 1. $ forward 90 degrees
 DRF-E electron ENERGY-FLUX
 DRF-E positron ENERGY-FLUX

 NUMBER = BC_EP1
 boundary COUNTS 11 12 1256.64
 MASK-A 1. 0. 0.  0. 1. $ forward 90 degrees
 MASK-E electron 0. 0.
 MASK-E positron 0. 0.
 DRF-E photon ENERGY-FLUX

 NUMBER = BC_ET2
 boundary COUNTS 13 14 1256.64
 MASK-E photon 0. 0.
 MASK-A 1. 0. 0.  0. 1. $ forward 90 degrees
 DRF-E electron ENERGY-FLUX
 DRF-E positron ENERGY-FLUX

 NUMBER = BC_EP2
 boundary COUNTS 13 14 1256.64
 MASK-E electron 0. 0.
 MASK-E positron 0. 0.
 MASK-A 1. 0. 0.  0. 1. $ forward 90 degrees
 DRF-E photon ENERGY-FLUX

 NUMBER = BC_ET3
 boundary COUNTS 15 16 1256.64
 MASK-E photon 0. 0.
 MASK-A 1. 0. 0.  0. 1. $ forward 90 degrees
 DRF-E electron ENERGY-FLUX
 DRF-E positron ENERGY-FLUX

 NUMBER = BC_EP3
 boundary COUNTS 15 16 1256.64
 MASK-E electron 0. 0.
 MASK-E positron 0. 0.
```

MASK-A 1. 0. 0. 0. 1. $ forward 90 degrees
DRF-E photon ENERGY-FLUX

NUMBER = BC_ET4
boundary COUNTS 17 18 1256.64
MASK-E photon 0. 0.
MASK-A 1. 0. 0. 0. 1. $ forward 90 degrees
DRF-E electron ENERGY-FLUX
DRF-E positron ENERGY-FLUX

NUMBER = BC_EP4
boundary COUNTS 17 18 1256.64
MASK-E electron 0. 0.
MASK-E positron 0. 0.
MASK-A 1. 0. 0. 0. 1. $ forward 90 degrees
DRF-E photon ENERGY-FLUX

NUMBER = BC_ET5
boundary COUNTS 19 20 1256.64
MASK-E photon 0. 0.
MASK-A 1. 0. 0. 0. 1. $ forward 90 degrees
DRF-E electron ENERGY-FLUX
DRF-E positron ENERGY-FLUX

NUMBER = BC_EP5
boundary COUNTS 19 20 1256.64
MASK-E electron 0. 0.
MASK-E positron 0. 0.
MASK-A 1. 0. 0. 0. 1. $ forward 90 degrees
DRF-E photon ENERGY-FLUX

NUMBER = BC_PR1
boundary 11 12 1256.64
DRF-E PHOTON
0 0
1.2170097471874737 0
2.5442639957812103 0
3.7907809901561578 0
4.989552233124842 0
6.2655777246872635 0
7.493857464843422 0
7.815665078462792 0
7.985224742018395 0
8.07803307224743 0
8.164977195790655 0

8.20374657900548	0
8.240600507639963	0
8.260911536367464	0
8.283081952895046	0.00011754828065558348
8.321949299822233	0.00011943728638238992
8.494846818945721	0.00012822244523190657
8.799391453593318	0.00014535150536072768
9.41909328208169	0.0001880894876475661
10.079722176874318	0.00024910616778481943
10.75418287738225	0.0003349536100510097
11.389561397342792	0.00044735271022243743
12.022018453194526	0.0006028755402182246
12.60390911499874	0.0007987864215082081
13.196882852741163	0.0010639763633774005
13.847765329842161	0.0014313384671521664
14.513830120524096	0.001833153662925411
14.829278212764857	0.0019915676107698237
14.968003818866986	0.0020471092359024864
15.04698322238015	0.0020739469891056105
15.121130041873057	0.0020957051168555116
15.197385237925568	0.0021144270746912444
15.267301997141212	0.0021282111759275764
15.342031970948879	0.002139270843003802
15.381275032461492	0.0021435368568044266
15.422591322840754	0.002146873594072203
15.461816509848765	0.00214894421444449
15.483772004137652	0.0021496372983404667
15.503721451206825	0.0021499778607343752
15.542548100634637	0.0021498544999071717
15.57920291614924	0.002148791226817558
15.599977543929535	0.0021477837765068266
15.621972024779005	0.002146400685093102
15.661405636795255	0.0021431143575068195
15.70383939077595	0.0021384385479204563
15.750516621096045	0.002131960170982028
15.828115500863749	0.002118197250028201
15.89901914836615	0.002102503337501692
16.058554587560085	0.002057252645212707
16.346749002497692	0.0019470389715399558
17.599215680778272	0.0013327682651638672
18.2314492892232	0.001070265750068613
18.803936607652588	0.0008817179373554943
19.42485600832214	0.0007226519740441892
20.085911783120643	0.0005936174404544497
20.6933886228119	0.0005023249259158961

21.34964970436991	0.00042525463748209957
21.966594179707837	0.0003679708912391051
22.642896122806647	0.00031773209716946034
23.88839678983712	0.0002492659664867768
24.504165885987742	0.0002235972730170549
25.16340595405507	0.00020045860608997596
26.467923615460492	0.0001645333006086514
27.72469552545965	0.00013872669273265028
28.933721684052546	0.0001195032464059864
29.99999875	0.00010585298010795054

NUMBER = BC_PR2
boundary 13 14 1256.64
DRF-E PHOTON

0	0
1.2170097471874737	0
2.5442639957812103	0
3.7907809901561578	0
4.989552233124842	0
6.2655777246872635	0
7.493857464843422	0
7.815665078462792	0
7.985224742018395	0
8.07803307224743	0
8.164977195790655	0
8.20374657900548	0
8.240600507639963	0
8.260911536367464	0
8.283081952895046	0.00011754828065558348
8.321949299822233	0.00011943728638238992
8.494846818945721	0.00012822244523190657
8.799391453593318	0.00014535150536072768
9.41909328208169	0.0001880894876475661
10.079722176874318	0.00024910616778481943
10.75418287738225	0.0003349536100510097
11.389561397342792	0.00044735271022243743
12.022018453194526	0.0006028755402182246
12.60390911499874	0.0007987864215082081
13.196882852741163	0.0010639763633774005
13.847765329842161	0.0014313384671521664
14.513830120524096	0.001833153662925411
14.829278212764857	0.0019915676107698237
14.968003818866986	0.0020471092359024864
15.04698322238015	0.0020739469891056105
15.121130041873057	0.0020957051168555116

15.197385237925568	0.0021144270746912444
15.267301997141212	0.0021282111759275764
15.342031970948879	0.002139270843003802
15.381275032461492	0.0021435368568044266
15.422591322840754	0.002146873594072203
15.461816509848765	0.00214894421444449
15.483772004137652	0.0021496372983404667
15.503721451206825	0.0021499778607343752
15.542548100634637	0.0021498544999071717
15.57920291614924	0.002148791226817558
15.599977543929535	0.0021477837765068266
15.621972024779005	0.002146400685093102
15.661405636795255	0.0021431143575068195
15.70383939077595	0.0021384385479204563
15.750516621096045	0.002131960170982028
15.828115500863749	0.002118197250028201
15.89901914836615	0.002102503337501692
16.058554587560085	0.002057252645212707
16.346749002497692	0.0019470389715399558
17.599215680778272	0.0013327682651638672
18.2314492892232	0.001070265750068613
18.803936607652588	0.0008817179373554943
19.42485600832214	0.0007226519740441892
20.085911783120643	0.0005936174404544497
20.6933886228119	0.000502324925915896 1
21.34964970436991	0.00042525463748209957
21.966594179707837	0.0003679708912391051
22.642896122806647	0.00031773209716946034
23.88839678983712	0.0002492659664867768
24.504165885987742	0.0002235972730170549
25.16340595405507	0.00020045860608997596
26.467923615460492	0.0001645333006086514
27.72469552545965	0.00013872669273265028
28.933721684052546	0.0001195032464059864
29.99999875	0.00010585298010795054

NUMBER = BC_PR3
boundary 15 16 1256.64
DRF-E PHOTON

0	0
1.2170097471874737	0
2.5442639957812103	0
3.7907809901561578	0
4.989552233124842	0
6.2655777246872635	0

7.493857464843422	0
7.815665078462792	0
7.985224742018395	0
8.07803307224743	0
8.164977195790655	0
8.20374657900548	0
8.240600507639963	0
8.260911536367464	0
8.283081952895046	0.00011754828065558348
8.321949299822233	0.00011943728638238992
8.494846818945721	0.00012822244523190657
8.799391453593318	0.00014535150536072768
9.41909328208169	0.0001880894876475661
10.079722176874318	0.00024910616778481943
10.75418287738225	0.0003349536100510097
11.389561397342792	0.00044735271022243743
12.022018453194526	0.0006028755402182246
12.60390911499874	0.0007987864215082081
13.196882852741163	0.0010639763633774005
13.847765329842161	0.0014313384671521664
14.513830120524096	0.001833153662925411
14.829278212764857	0.0019915676107698237
14.968003818866986	0.0020471092359024864
15.04698322238015	0.0020739469891056105
15.121130041873057	0.0020957051168555116
15.197385237925568	0.0021144270746912444
15.267301997141212	0.0021282111759275764
15.342031970948879	0.002139270843003802
15.381275032461492	0.0021435368568044266
15.422591322840754	0.002146873594072203
15.461816509848765	0.00214894421444449
15.483772004137652	0.0021496372983404667
15.503721451206825	0.0021499778607343752
15.542548100634637	0.0021498544999071717
15.57920291614924	0.002148791226817558
15.599977543929535	0.0021477837765068266
15.621972024779005	0.002146400685093102
15.661405636795255	0.0021431143575068195
15.70383939077595	0.0021384385479204563
15.750516621096045	0.002131960170982028
15.828115500863749	0.002118197250028201
15.89901914836615	0.002102503337501692
16.058554587560085	0.002057252645212707
16.346749002497692	0.0019470389715399558
17.599215680778272	0.0013327682651638672

18.2314492892232	0.001070265750068613
18.803936607652588	0.0008817179373554943
19.42485600832214	0.0007226519740441892
20.085911783120643	0.0005936174404544497
20.6933886228119	0.0005023249259158961
21.34964970436991	0.00042525463748209957
21.966594179707837	0.0003679708912391051
22.642896122806647	0.00031773209716946034
23.88839678983712	0.0002492659664867768
24.504165885987742	0.0002235972730170549
25.16340595405507	0.00020045860608997596
26.467923615460492	0.0001645333006086514
27.72469552545965	0.00013872669273265028
28.933721684052546	0.0001195032464059864
29.99999875	0.00010585298010795054

NUMBER = BC_PR4
boundary 17 18 1256.64
DRF-E PHOTON
0 0

1.2170097471874737	0
2.5442639957812103	0
3.7907809901561578	0
4.989552233124842	0
6.2655777246872635	0
7.493857464843422	0
7.815665078462792	0
7.985224742018395	0
8.07803307224743	0
8.164977195790655	0
8.20374657900548	0
8.240600507639963	0
8.260911536367464	0
8.283081952895046	0.00011754828065558348
8.321949299822233	0.00011943728638238992
8.494846818945721	0.00012822244523190657
8.799391453593318	0.00014535150536072768
9.41909328208169	0.0001880894876475661
10.079722176874318	0.00024910616778481943
10.75418287738225	0.0003349536100510097
11.389561397342792	0.00044735271022243743
12.022018453194526	0.0006028755402182246
12.60390911499874	0.0007987864215082081
13.196882852741163	0.0010639763633774005
13.847765329842161	0.0014313384671521664

14.513830120524096	0.001833153662925411
14.829278212764857	0.0019915676107698237
14.968003818866986	0.0020471092359024864
15.04698322238015	0.0020739469891056105
15.121130041873057	0.0020957051168555116
15.197385237925568	0.0021144270746912444
15.267301997141212	0.0021282111759275764
15.342031970948879	0.002139270843003802
15.381275032461492	0.0021435368568044266
15.422591322840754	0.002146873594072203
15.461816509848765	0.00214894421444449
15.483772004137652	0.0021496372983404667
15.503721451206825	0.0021499778607343752
15.542548100634637	0.0021498544999071717
15.57920291614924	0.002148791226817558
15.599977543929535	0.0021477837765068266
15.621972024779005	0.002146400685093102
15.661405636795255	0.0021431143575068195
15.70383939077595	0.0021384385479204563
15.750516621096045	0.002131960170982028
15.828115500863749	0.002118197250028201
15.89901914836615	0.002102503337501692
16.058554587560085	0.002057252645212707
16.346749002497692	0.0019470389715399558
17.599215680778272	0.0013327682651638672
18.2314492892232	0.001070265750068613
18.803936607652588	0.0008817179373554943
19.42485600832214	0.0007226519740441892
20.085911783120643	0.0005936174404544497
20.6933886228119	0.0005023249259158961
21.34964970436991	0.00042525463748209957
21.966594179707837	0.0003679708912391051
22.642896122806647	0.00031773209716946034
23.88839678983712	0.0002492659664867768
24.504165885987742	0.0002235972730170549
25.16340595405507	0.00020045860608997596
26.467923615460492	0.0001645333006086514
27.72469552545965	0.00013872669273265028
28.933721684052546	0.0001195032464059864
29.99999875	0.00010585298010795054

NUMBER = BC_PR5
boundary 19 20 1256.64
DRF-E PHOTON
0 0

1.2170097471874737	0
2.5442639957812103	0
3.7907809901561578	0
4.989552233124842	0
6.2655777246872635	0
7.493857464843422	0
7.815665078462792	0
7.985224742018395	0
8.07803307224743	0
8.164977195790655	0
8.20374657900548	0
8.240600507639963	0
8.260911536367464	0
8.283081952895046	0.00011754828065558348
8.321949299822233	0.00011943728638238992
8.494846818945721	0.00012822244523190657
8.799391453593318	0.00014535150536072768
9.41909328208169	0.0001880894876475661
10.079722176874318	0.00024910616778481943
10.75418287738225	0.0003349536100510097
11.389561397342792	0.00044735271022243743
12.022018453194526	0.0006028755402182246
12.60390911499874	0.0007987864215082081
13.196882852741163	0.0010639763633774005
13.847765329842161	0.0014313384671521664
14.513830120524096	0.001833153662925411
14.829278212764857	0.0019915676107698237
14.968003818866986	0.0020471092359024864
15.04698322238015	0.0020739469891056105
15.121130041873057	0.0020957051168555116
15.197385237925568	0.0021144270746912444
15.267301997141212	0.0021282111759275764
15.342031970948879	0.002139270843003802
15.381275032461492	0.0021435368568044266
15.422591322840754	0.002146873594072203
15.461816509848765	0.00214894421444449
15.483772004137652	0.0021496372983404667
15.503721451206825	0.0021499778607343752
15.542548100634637	0.0021498544999071717
15.57920291614924	0.002148791226817558
15.599977543929535	0.0021477837765068266
15.621972024779005	0.002146400685093102
15.661405636795255	0.0021431143575068195
15.70383939077595	0.0021384385479204563
15.750516621096045	0.002131960170982028

15.828115500863749	0.002118197250028201
15.89901914836615	0.002102503337501692
16.058554587560085	0.002057252645212707
16.346749002497692	0.0019470389715399558
17.599215680778272	0.0013327682651638672
18.2314492892232	0.001070265750068613
18.803936607652588	0.0008817179373554943
19.42485600832214	0.0007226519740441892
20.085911783120643	0.0005936174404544497
20.6933886228119	0.0005023249259158961
21.34964970436991	0.00042525463748209957
21.966594179707837	0.0003679708912391051
22.642896122806647	0.00031773209716946034
23.88839678983712	0.0002492659664867768
24.504165885987742	0.0002235972730170549
25.16340595405507	0.00020045860608997596
26.467923615460492	0.0001645333006086514
27.72469552545965	0.00013872669273265028
28.933721684052546	0.0001195032464059864
29.99999875	0.00010585298010795054

END

Appendix B

Results from a 100,000 particle run with 50 137Cs disks (20-cm radius, 0.1-cm thick) separated from each other by 5 cm vacuum.

Disk Number	e+, e- Energy Out Back Surface (MeV/(src)	Photon Energy Out Back Surface (Mev/src)	Unscattered 14-Mev Photon Fraction	Conversion Reactions/src
1	0.412	13.5	0.96	7.31×10^{-4}
2	0.619	13.0	0.92	7.01×10^{-4}
3	0.683	12.6	0.88	6.73×10^{-4}
4	0.671	12.2	0.85	6.47×10^{-4}
5	0.660	11.8	0.81	6.21×10^{-4}
6	0.644	11.4	0.78	5.96×10^{-4}
7	0.626	11.0	0.75	5.71×10^{-4}
8	0.610	10.6	0.72	5.48×10^{-4}
9	0.576	10.2	0.69	5.26×10^{-4}
10	0.539	9.83	0.66	5.05×10^{-4}
11	0.516	9.47	0.63	4.85×10^{-4}
12	0.490	9.13	0.61	4.66×10^{-4}
13	0.467	8.80	0.58	4.48×10^{-4}
14	0.454	8.47	0.56	4.30×10^{-4}
15	0.444	8.15	0.54	4.13×10^{-4}
16	0.431	7.84	0.51	3.97×10^{-4}
17	0.405	7.55	0.49	3.81×10^{-4}
18	0.401	7.24	0.47	3.65×10^{-4}
19	0.388	6.96	0.45	3.50×10^{-4}
20	0.364	6.70	0.43	3.36×10^{-4}
21	0.353	6.43	0.42	3.22×10^{-4}
22	0.347	6.17	0.40	3.09×10^{-4}
23	0.329	5.93	0.38	2.96×10^{-4}
24	0.312	5.70	0.37	2.84×10^{-4}
25	0.304	5.47	0.35	2.72×10^{-4}
26	0.276	5.26	0.34	2.62×10^{-4}
27	0.264	5.06	0.32	2.52×10^{-4}
28	0.259	4.86	0.31	2.42×10^{-4}
29	0.255	4.66	0.30	2.32×10^{-4}
30	0.246	4.48	0.29	2.22×10^{-4}
31	0.234	4.30	0.27	2.13×10^{-4}
32	0.215	4.14	0.26	2.05×10^{-4}
33	0.208	3.97	0.25	1.97×10^{-4}
34	0.198	3.82	0.24	1.90×10^{-4}
35	0.192	3.67	0.23	1.82×10^{-4}
36	0.188	3.52	0.22	1.75×10^{-4}
37	0.181	3.38	0.21	1.68×10^{-4}
38	0.178	3.24	0.21	1.60×10^{-4}
39	0.168	3.12	0.20	1.54×10^{-4}
40	0.161	2.99	0.19	1.48×10^{-4}
41	0.155	2.87	0.18	1.42×10^{-4}
42	0.148	2.76	0.17	1.36×10^{-4}

43	0.145	2.64	0.17	1.31×10^{-4}
44	0.141	2.54	0.16	1.25×10^{-4}
45	0.132	2.43	0.15	1.20×10^{-4}
46	0.119	2.34	0.15	1.16×10^{-4}
47	0.120	2.25	0.14	1.11×10^{-4}
48	0.116	2.16	0.14	1.06×10^{-4}
49	0.111	2.07	0.13	1.02×10^{-4}
50	0.102	1.99	0.12	9.82×10^{-5}